Mechanotunable Surface Lattice Resonances in the Visible Optical Range by Soft Lithography Templates and Directed Self-Assembly

Vaibhav Gupta,[†,∥] Patrick T. Probst,[†,‡,∥] Fabian R. Goßler,[†] Anja Maria Steiner,[†] Jonas Schubert,[†,‡,§] Yannic Brasse,[†,‡] Tobias A. F. König,*[†,‡] and Andreas Fery*[†,‡,§]

[†]Institute for Physical Chemistry and Polymer Physics, Leibniz-Institut für Polymerforschung Dresden e.V., Hohe Str. 6, 01069 Dresden, Germany

[‡]Cluster of Excellence Center for Advancing Electronics Dresden (cfaed) and [§]Physical Chemistry of Polymeric Materials, Technische Universität Dresden, 01069 Dresden, Germany

S *Supporting Information*

ABSTRACT: We demonstrate a novel colloidal self-assembly approach toward obtaining mechanically tunable, cost-efficient, and low-loss plasmonic nanostructures that show pronounced optical anisotropy upon mechanical deformation. Soft lithography and template-assisted colloidal self-assembly are used to fabricate a stretchable periodic square lattice of gold nanoparticles on macroscopic areas. We stress the impact of particle size distribution on the resulting optical properties. To this end, lattices of narrowly distributed particles (∼2% standard deviation in diameter) are compared with those composed of polydisperse ones (∼14% standard deviation). The enhanced particle quality sharpens the collective surface lattice resonances by 40% to achieve a full width at half-maximum as low as 16 nm. This high optical quality approaches the theoretical limit for this system, as revealed by electromagnetic simulations. One hundred stretching cycles demonstrate a reversible transformation from a square to a rectangular lattice, accompanied by polarization-dependent optical properties. On the basis of these findings we envisage the potential applications as strain sensors and mechanically tunable filters.

KEYWORDS: stretchable optics, strain-sensing, surface lattice resonance, Bragg reflector, template-assisted self-assembly
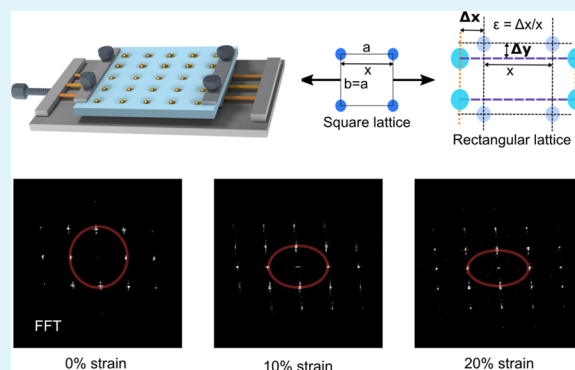
INTRODUCTION

Plasmonic resonances of metallic nanoparticles are of broad interest because of their strong interaction with light and their energy confinement at sub-wavelength scales. Light interaction induces collective oscillation of free electrons commonly known as localized surface plasmon resonance (LSPR). Spectral properties of such modes can be engineered by varying the nanoparticle composition, size or shape, and the surrounding refractive index.[1] For photonic and optical applications, it is desirable to achieve high optical quality and wide optical tunability simultaneously. The quality factor is defined by the ratio of the resonance wavelength to the resonance width. One effective approach toward obtaining high optical quality is the interference between a plasmon mode and a Bragg grating mode, also known as symmetry breaking or Fano resonance.[2,3] The arising surface lattice resonance (SLR) yields coherence to the system by confining the high electromagnetic field in the lattice plane.[4] Whereas typical LSPR exhibits a full width at half-maximum (fwhm) of >80 nm, for SLR the spectral width is drastically reduced, down to 1−2 nm.[5]

In order to steer this lattice plasmonic resonance to the visible wavelength (λ), an energetic overlap between the Bragg mode and the particle plasmon resonance is necessary. In the first order and at normal incidence, the mode occurs at λn (n as environmental refractive index).[6] To cover the entire visible area, the size of the particles and the lattice periodicity must be adjusted accordingly.[7] Such SLR response in the visible wavelength range was demonstrated for a lattice of aluminum rectangles fabricated by electron beam lithography.[8] In those examples, lithography methods were employed, which require masks and etching processes. Thus, fabrication becomes costly and highly energy-consumptive. Colloidal self-assembly can be a more cost-efficient and ecofriendly alternative, and renders SLR on cm² areas easily accessible. For example, non-close hexagonally packed particle arrays supporting SLR can be readily generated by floating plasmonic core−shell nano-particles at the water−air interface.[9] In this system, the temperature-induced change in the refractive index of the
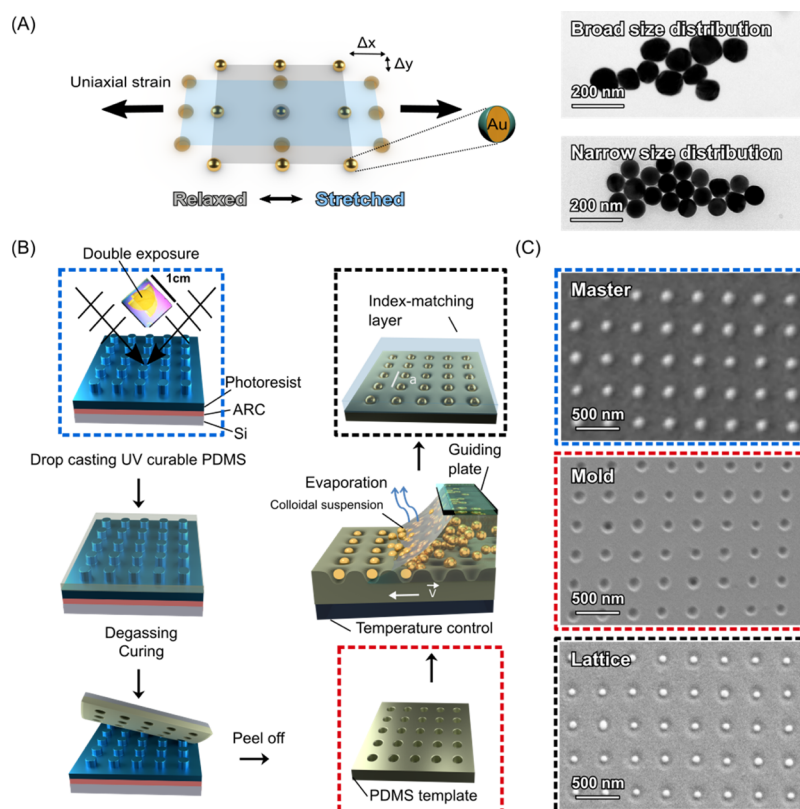
Figure 1. Soft lithography template fabrication for directed self-assembly. (A) Scheme of a stretchable 2D plasmonic lattice under uniaxial strain. Corresponding TEM images of two particle systems with broad and narrow particle size distribution. (B) Scheme represents the fabrication of a stretchable 2D lattice using a combination of LIL, soft molding, and directed self-assembly of plasmonic nanoparticles. ARC: anti-reflective coating. (C) SEM images of the fabricated nanopillars master, nanoholes array, and 2D plasmonic lattice (narrow size distribution). Dashed frames in pictorial representation correspond to the SEM image.

hydrogel shell additionally allows a reversible 50 nm shift of the hybridized mode with a line width of 50 nm.

Recently, mechanical deformation of plasmonic arrays sparked research interest as an alternative stimulus for spectral tuning.[5] Odom and co-workers showed that optimum conditions for lasing can be achieved by mechanical tuning.[10] As well, we showed in earlier work that colloidal linear particle assembly can be split into plasmonic oligomers, resulting in strain sensitivity and potential applications in sensing.[11] The colloidal approach is particularly well suited for creating mechanically tunable assemblies as particles can be directly transferred to the target substrate or embedded in elastomers. For precise strain-induced tuning of optical properties, it is mandatory to address specific lattice orientations consistently over the whole substrate. Therefore, defect-free templates molded from electron beam masters are commonly used in capillarity-assisted particle assembly of two-dimensional (2D) lattices.[12,13] Porous anodic alumina[14] or laser interference lithography (LIL)[15] can be a better scalable alternative. In contrast, hexagonal assemblies produced template-free at the water−air or liquid−liquid interface suffer from differently oriented domains. The variation in strain-induced lattice deformation from domain to domain would lead to a broad averaged SLR peak.

In this work, we combine the top-down method soft lithography and the bottom-up method template-assisted self-assembly (TASA) as facile and scalable fabrication methods to generate a mechanically tunable SLR. Flexible nature of the metasurface can overcome the optical cavity design limitation

by creating real-time tunable high-quality mode. To design the collective optical properties for the visible wavelength regime, we use electromagnetic finite element simulations. After realizing the square lattice of gold nanospheres assembled inside an elastomeric template, the sharp spectral features, modulated by mechanical stresses, are quantified using conventional UV−vis spectroscopy. Both our theoretical and experimental results stress the importance of particle size polydispersity for the quality of the collective SLR mode. Our approach of flexible and tunable high-quality plasmonic lattice paves the way for cost-effective next-generation optical and photonic devices.

■ RESULTS AND DISCUSSION

We discuss a 2D square plasmonic lattice embedded in polydimethylsiloxane (PDMS) that shows a dynamic tuning of lattice constants under mechanical deformation. Because of a Poisson's ratio (which is the negative of the ratio of transverse to axial strain) of 0.5, stretching in the x-direction results in a reduction in the y-direction.[11] Consequently, applying a uniaxial strain transforms the system from a square to a rectangular lattice (Figure 1A). Generally, a non-stretched plasmonic square lattice enables coupling between single-particle LSPR and degenerate 2D Bragg diffraction to produce two hybridized modes.[16] Upon deformation into a rectangular lattice, two different Bragg modes (along the x- and y-directions) arise, which interact with the LSPR and allow switchable hybrid modes with polarization dependence.[10]
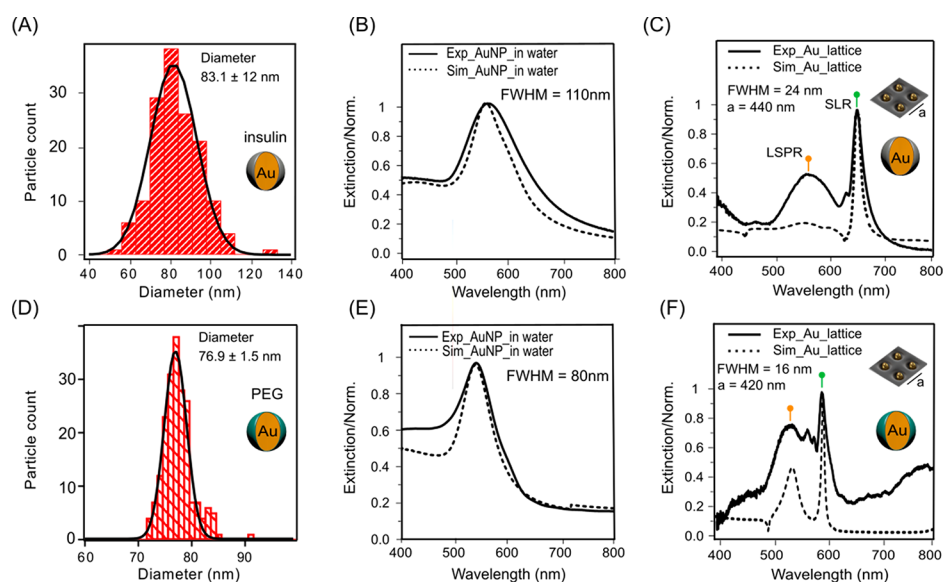
Figure 2. From various colloidal particle systems to SLR. (A,D) Size distribution of broadly/narrowly distributed gold nanoparticles coated with insulin and PEG, respectively. (B,E) Corresponding experimental and simulated extinction spectra in water. (C,F) Simulated and measured extinction of a 2D plasmonic lattice at periodicity (a = 440 nm) for a broad case and (a = 420 nm) for a narrow case. To reflect the particle polydispersity, the simulated spectra were averaged for different particle diameters.

In order to obtain high-quality modes, it is vital to maintain energetic stability and order in the system.[17,18] To achieve those essentials, we followed a soft lithography fabrication approach to create a square lattice of well-defined periodicity over cm[2] areas (Figure 1B). This method starts with a double LIL exposure to fabricate the nanopillar master on a photoresist-coated silicon wafer. Negative replication by a soft lithography molding step produces a nanohole structure (nanohole array from UV-curable PDMS). More details about the LIL setup are shown in Supporting Information Text T1 and Figure S1. This flexible template was used for capillarity-assisted assembly to align the colloidal plasmonic nanoparticles in a 2D square lattice. Briefly, a droplet of nanoparticle suspension was dragged across the topographical template. The hole dimensions were chosen (120 nm diameter and ∼70 nm depth, see also Figure S2) such that only one particle fits into it. A high filling rate can be achieved at the same time (see Figure 1C).[13] At the receding meniscus, the particles concentrate facilitated by evaporation-driven convection. This local accumulation reduces the Brownian motion of nanoparticles and thereby increases the probability of particles being deposited inside the features. Net repulsive particle–substrate interaction and good colloidal stabilization of particles provided by surface modification prevent random sequential adsorption to the substrate and irreversible aggregation, respectively. Precise tuning of contact angle and surface tension balances the components of the capillary force at the meniscus acting parallel and normal to the substrate to drag the gold nanoparticles along and only allow deposition where they feel a sidewall of the topographical features counteracting this motion (more details are in Supporting Information Text T2).[19] As a big advantage of this assembly method, the assembly area is only limited by template size and reservoir of colloidal particle solution. It was already demonstrated that the latter limitation can be overcome by a continuous microfluidic feed of suspension.[20]

To investigate the influence of particle size distribution on SLR quality, square lattices of two different particle systems

were fabricated: one with a broad particle size distribution and one with a narrow size distribution that shows an eightfold smaller standard deviation (Figure 2A,D). Citrate- and surfactant-stabilized synthesis routes were used to produce broad and narrow size distributions, respectively (see the Experimental Section for more details). The low-molecular-weight ligands from syntheses were exchanged against insulin and polyethylene glycol (PEG) to demonstrate the tolerance of the employed assembly technique concerning different surface chemistries. Indeed, the achieved filling rates are comparable, being 81 and 79%, respectively, as evaluated from 150 × 150 μm[2] scanning electron microscopy (SEM) images (more details are in Supporting Information Text T4). The good periodic order of the plasmonic grating was characterized employing the radial distribution function as evaluated from SEM (more details are in Supporting Information Text T5). Moreover, the utilized coatings provide good biocompatibility and help integration in biomedical sensing applications.[21,22] For technical reasons the broad particle size distribution particles were arranged in a 440 nm and the narrow particle size distribution particles were assembled in a 420 nm square lattice. Finally, the plasmonic lattice was index-matched by spin-coating an ultraviolet (UV) curable PDMS layer. Embedding of particles leads to the same wavelength for the wavefront propagation in substrate and superstrate, which enhances the in-plane coupling of the SLR.

The spectra of single particles with LSPR at 560 nm (broad) and 540 nm (narrow) in aqueous solution were reproduced by finite-difference time-domain (FDTD) simulations (Figure 2B,E). A summary of optical properties resulting from the two particle distributions is presented in Supporting Information Table S1. To reflect the particle polydispersity, the simulated data for the broad size distribution were averaged over several spectra of varying particle size. Because of the periodic arrangement, the nanoparticles couple with each other coherently and an SLR mode arises for both particle kinds (Figure 2C,F). A detailed explanation of SLR is given in Supporting Information T3. However, with narrowly dis-
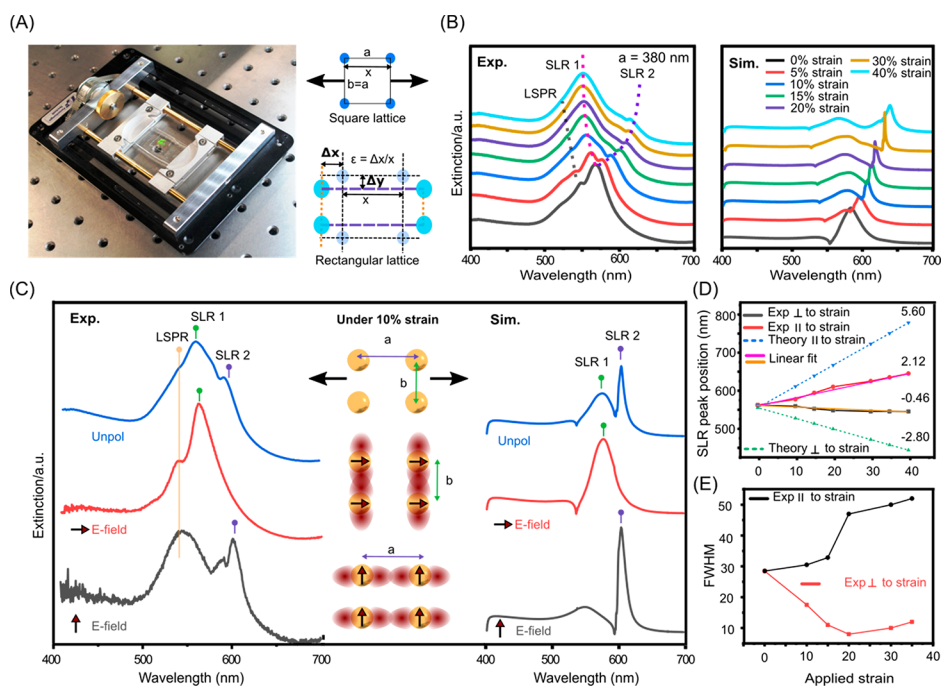
Figure 3. Mechanotunable SLR. (A) Photograph of the stretching device with a clamped sample in the center and schematic of the square lattice under uniaxial strain. (B) Experimental and simulated spectra of the gold nanoparticle lattice under various strains (considering partial force transfer in simulations). (C) Experimental and simulated polarization-dependent selective reading of the lattice resonance modes. (D) Comparison between theoretically expected (100% force transfer) and experimentally obtained SLR peak positions. (E) fwhm of the SLR peaks for various strains.

tributed particles (Figure 2F), the fwhm is reduced from 24 to 16 nm (Q-factor $\lambda/\Delta\lambda$ from 27 to 36) as compared to more polydisperse particles (Figure 2C). This highlights the importance of particle quality, as expected from the corresponding simulated spectra (Figure 2C,F). Note that the mode structure is nicely reproduced by simulations for the narrow size distribution (Figure 2F), whereas the LSPR is only weakly reproduced for the broader case (Figure 2C). The larger size distribution and scattering cross section result in a broad LSPR that is less pronounced as compared to the SLR peak. It is important to mention that in simulations an infinite lattice is considered, whereas an experiment averaging over a 12 mm² area reflects variations in particle coverage. Therefore, the ratio of SLR to LSPR extinction is larger in simulations as compared to experiments. We also performed the mean square error (MSE) calculations. The MSE is defined as the average squared difference of the normalized extinction values between the simulation data and what is measured experimentally. The MSE value in the case of broadly distributed gold nanoparticle lattice SLR is 0.11 and for the narrow size distribution it is 0.13. This leads to the fact that experimental spectra match nearly perfectly with simulations. The small oscillation between LSPR and SLR represents the Rayleigh anomaly. This is the wavelength where diffraction turns from being evanescent to radiative.[6] In general, a larger period (440 nm) is expected to produce a narrower SLR as compared to 420 nm because of less overlap with plasmonic losses. The fact that the narrowly distributed particles show a smaller fwhm even for a less optimal 420 nm lattice emphasizes the benefits of mono-disperse building blocks. Please note that despite the different synthesis routes used, both particle types are monocrystalline and consequently show comparable plasmonic damping. Furthermore, insulin and PEG coating of particles produce a

similar dielectric environment as both represent organic ligands.

In order to modulate the SLR mode at normal incidence, we benefit from the flexible nature of the UV-PDMS substrate (Figure 3). We discuss here the mechanical tunability only with the narrow particle size distribution particles and compared two different periodicities, 420 and 380 nm. Stretching experiments for broadly distributed particles at a periodicity of 440 nm are provided in Supporting Information S7. The lattice constant of our particle array can be varied in situ by straining the substrate uniaxially. Because of its centimeter square dimensions, the optical properties of the final plasmonic lattice could be studied using conventional UV−vis spectroscopy with a beam size of 3 × 4 mm². Figure 3A shows the photograph of a home-built stretching device. Increasing the strain gradually from 0 to 40% transforms the square lattice into a rectangular one with lattice constant a (along the applied strain direction) and b (along the perpendicular direction). Two different lattice constants in the x- and y-directions result in two different SLR modes. Because of the strain-induced non-degeneration, one of the SLR shifts toward higher wavelengths (violet color marker in Figure 3B), whereas the other one is blue-shifted (pink color marker) for unpolarized light illumination. We found that the macroscopically applied strain was only partially transferred to the lattice (more details below). Therefore, the simulated spectra displayed in the right panel of Figure 3B were calculated for the effective lattice constraints as derived from the experimental spectra. The experimentally observed spectral shifts are in good agreement with FDTD simulations. In general, SLR1 is broader as compared to SLR2 because of the reduced plasmonic damping of gold for larger wavelengths in the visible wavelength range.[7] Moreover, the Q-factor of SLR is
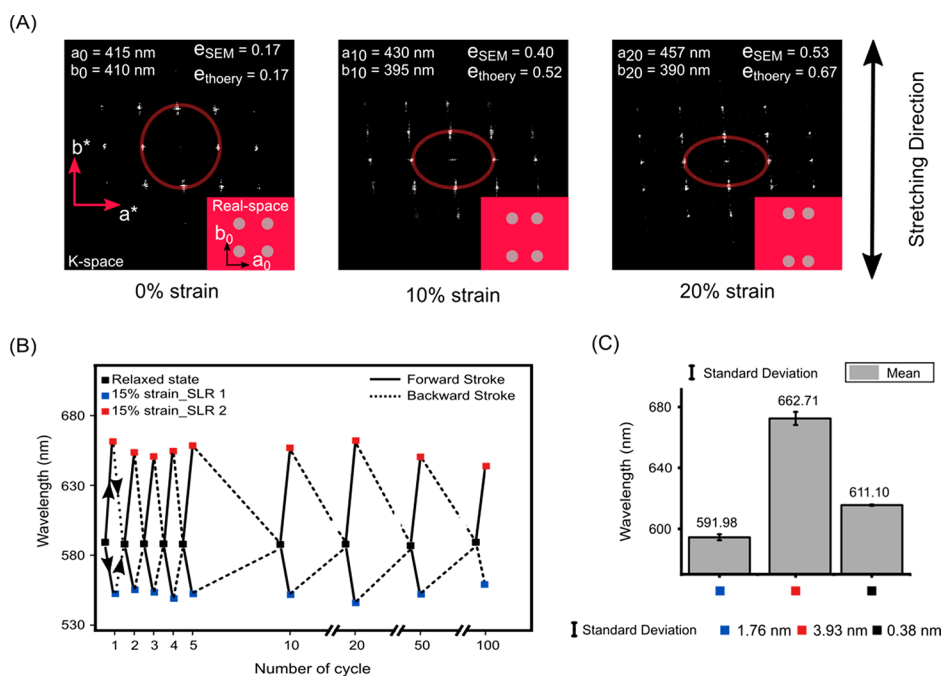
Figure 4. Evaluation of strain transfer. (A) 2D fast Fourier transform (FFT) of 0, 10, and 20% strain SEM images. a_i, b_i and a_i^* b_i^* are the lattice constants in real space and k-space respectively, with i giving the applied strain in percent. (B) Stretch and relax cycles of a plasmonic lattice ($a = 420$ nm) plotted against SLR peaks for 15% strain. (C) Mean value and standard deviation in SLR peak positions are shown for relaxed and stretched cases. Abbreviation e represents the ellipticity of the ellipse.

an interplay between the single particle scattering cross section and the Bragg mode. The low-quality SLR1 shows a significant overlap with the broad LSPR mode for all applied strains. In contrast, the overlap of SLR2 gradually decreases when red-shifting with increasing strain. A strain of 30% (20% in experiments, Figure 3E) represents an optimal balance between LSPR and Bragg modes. The reduced overlap accompanied with less plasmonic character produces a very sharp peak SLR2. When increasing the strain further, SLR2 moves out of the scattering cross section of the single particle, leading to peak broadening. This optimization by adjustment of periodicities of the lattice is explained theoretically in Supporting Information Text T3.

The two different SLR modes in rectangular lattices can be studied in more detail when using linearly polarized excitation, as depicted in Figure 3C for a 10% strain. Note that the SLR induced by polarization in the x-direction is at lower wavelengths as compared to the y-excitation. At first glance, this is counterintuitive as the periodicity in the x-direction is larger. However, this can be understood by considering every plasmonic particle as a dipole antenna. This effect is highlighted in the schematic illustration in Figure 3C. Excitation along the x-axis induces electron oscillations in the parallel orientation for each particle. Yet, these dipoles radiate the scattered light mainly perpendicular to the dipole moment. This concludes that the surface lattice mode always propagates normal to the incident E-field direction. Or, in other words, for an asymmetric lattice, the SLR mode is defined by the lattice constant which is normal to the incident polarization.[23]

As mentioned before, we see a deviation between macroscopically applied strain and effective deformation of the lattice. Figure 3D compares the strain-induced experimental peak shifts with the theoretical values (considering 100% transfer of applied strain and Poisson's ratio of 0.5). SLR1 is

modulated by strain parallel to the stretching direction, whereas the shift in SLR2 reflects the perpendicular strain. The comparison between the slopes (linear fit) of the strain-dependent SLR position for theory and experiment gives a measure for partial strain transfer. The ratio between slopes gives 37.8% transfer parallel to the stretching direction and 16.4% in the perpendicular direction (ratio of perpendicular/parallel 0.43). This is in good agreement with the in situ stretching results in dark-field microscopy (Supporting Information Figure S8). We attribute the partial transfer of strain to the creep of the polymer chains and deformation of the clamped region when applying a macroscopic strain. It is important to emphasize that the optical quality can be changed by the stretching (Figure 3E). In general, one of the resonance peaks undergoes a red shift, whereas the other one is blue-shifted under successively increased strain. As compared to a relaxed state, the coupling strength between LSPR and Bragg modes decreases under strain for the red-shifted SLR modes (narrow fwhm in the case of 30% strain). The blue-shifted SLR successively becomes broader in terms of line width (fwhm) because of increased overlap with the single particle scattering cross section that leads to more plasmonic losses. Depending on the application aspect, this gives freedom in terms of fwhm selection.

The optical analysis shows that the applied macroscopic strain can only be converted by about 38 and 16%. In order to justify this relationship, we have carried out SEM measurements of the strained samples (Figure 4). These measurements were performed for a plasmonic lattice constant of 420 nm. SEM images were analyzed with 2D FFT for 0, 10, and 20% strain. Evaluated lattice constants (a, b) in parallel and perpendicular with respect to the real space strain direction (black arrow) are shown in Figure 4A. In the relaxed state, the FFT shows that the lattice itself is not perfectly square. During the LIL fabrication, the samples are illuminated twice and

mechanically rotated 90°. Inaccuracies in the rotation can lead to a deviation in the lattice pattern. We compared the eccentricity values from theory and SEM to understand the deviation of the ellipse from being circular. Eccentricity values show a clear trend that UV-PDMS grating was stretched but the force transfer on to the particle grating was partial. In the case of 20% strain, the lattice constant in the strain direction changes from 415 to 457 nm. This translates to a 50% strain transfer as compared to theoretical values. Similarly, for perpendicular to the strain direction, only 24% of the strain was transferred. Finally, the stretching inside the SEM confirms that there is moderate force transferred from the macroscopic scale to the nanometer lattice deformation scale. The force cannot be implemented one to one probably because of the clamp holder. To stretch the PDMS, the material is squeezed at the clamp holder with an unrecognized force, which can cause the mismatch. Note that the deviation between SEM and optical spectrum data could also be because of the absence of the index matching layer during the SEM measurement. Nonuniform embedding leads to less frictional forces and more degree of freedom in terms of particle motion.

In order to confirm the robustness of the elastomeric plasmonic lattice, the sample was stretched and relaxed 100 times and the bright-field spectrum was measured after each cycle (Figure 4B). The maximum strain was kept to a constant value of 15% for all the cycles. The black color dots (relaxed state) in Figure 4B show that UV-PDMS recovers even after 100 cycles with a standard deviation of only 0.38 nm, as summarized in Figure 4C. The deviation in the values for SLR1 (blue dots) and SLR2 (red dots) is higher as compared to the relaxed state. This can be correlated with the manual handling of the stretching device.

■ CONCLUSIONS

In conclusion, we discussed the assembly of ordered nanoparticle arrays that show a narrow and mechanically tunable SLR over 100 cycles of deformations. The assembly relies on directed self-assembly of colloidal nanoparticles in templates formed by soft lithography. We showed the arrangement with broad/narrow particle size distribution and discussed their influence on the optical quality. The real-time mechanical tuning and accessibility of non-degenerated SLR modes hold great potential for plasmonic lasing,[24] biosensing,[25] or colorimetric sensors.[8] We show that the optical properties of the system change dramatically upon applying strain, as the array changes from a square lattice to a rectangular lattice. Importantly, the optical quality is not lost upon straining the system and the SLR peaks can be shifted over a wavelength range of 70 nm. Moreover, the uniaxially strained lattice opens up the possibility for introducing optical anisotropy. This scalable system with monocrystalline nanoparticle building blocks provides a platform to curb the rigid nature of optical systems and offers versatile plasmon mode engineering within flexible electronics. Finally, the rational design framework established also allows for extending the approach to supracolloidal structure (clusters, hetero-clusters, etc.).

■ EXPERIMENTAL SECTION

Template Fabrication. Nanopillars with various periodicities and diameters were fabricated with LIL using Lloyd's mirror setup. Further experimental details can be found in Supporting Information Text T1. A cleaned silicon wafer substrate (2.54 cm × 2.54 cm) was

first spin-coated with a back antireflection coating AZ BARLi II (70 nm in thickness). Further, a layer (214 nm thickness) of AZ MIR 701 14cp (Micro Chemicals GmbH) positive resist, 1 to 1 ratio diluted with ethyl L-lactate, was spin-coated (6000 rpm, 60 s) on top. The sample was exposed twice to the laser with 90° sample rotation. A wet chemical development process was used to etch the exposed resist in order to fabricate the pillars (master structures). The sample was immersed in AZ 726 MIF developer (Micro Chemicals GmbH) for 30 s followed by gentle rinsing with water and nitrogen drying. Soft lithography was employed to fabricate elastic molds of the as-prepared periodic nanostructures using silicone rubber PDMS, called UV-PDMS. We used two-component KER-4690 photo-curable PDMS (Shin Etsu & Micro Resist Technology GmbH) with a 1 to 1 mixing ratio. The mixture was stirred for 30 min through the magnetic stirring process and degassed for 20 min. The blend was drop-casted on the substrate, degassed again, and cured with a 365 nm UV lamp for 30 min. After the peel-off process possible remains of the photoresist were removed by rinsing with ethanol and drying with nitrogen.

Nanoparticle Synthesis. *Particle Synthesis of Broad Size Distribution.* Citrate-stabilized nanoparticles were prepared via seed-mediated growth synthesis.[26] The protein coating was prepared according to earlier published methods.[27−29] Briefly, 40 mL of the nanoparticle solution was added to a 4 mL 1 mg mL^{-1} insulin solution with 1% wt sodium citrate at pH 9 to generate the desired protein coating. The solution was allowed to incubate overnight. After fourfold centrifugation, the nanoparticles were analyzed with UV−vis and Libra 120 transmission electron microscopy (TEM). The nanoparticle size of 83.1 ± 12.2 nm was determined by statistical analysis of 150 particles.

Particle Synthesis of Narrow Size Distribution. Spherical gold nanoparticles capped by hexadecyltrimethylammonium chloride were synthesized by a seed-mediated growth process.[11] The resulting particles had a size of 76.9 ± 1.5 nm as determined by (TEM) statistics (at least 100 particles). Briefly, the PEG-stabilized particles were synthesized in three steps. First, so-called Wulff seeds are produced by reducing tetrachloroauric acid (HAuCl$_4$) with sodiumborohydrate (NaBH$_4$) in the presence of hexadecyltrimethylammonium bromide (CtaB). The obtained 2 nm large and single-crystalline particles are successively grown by two further synthesis steps until they reach the desired particle size. During the growing process, HAuCl$_4$, ascorbic acid, and CtaC serve as the Au precursor, reductant, and stabilizing agent. In order to guarantee kinetic control and thus control over the particle shape, a syringe pump system is used for the last growing step. The resulting particles were purified by centrifuge washing and set to a surfactant concentration of 2 mM. For the self-assembly step, a ligand exchange was performed from CtaC to PEG-6k-SH.[30]

Template-Assisted Colloidal Self-Assembly. Prior to the assembly experiment, the microscopy glass slide (Menzel) was hydrophobized via gas-phase deposition of trichloro(1*H*,1*H*,2*H*,2*H*-perfluorooctyl)silane (448931, Sigma-Aldrich) at 60 °C for 3 h. Using a custom-made setup, 15 μL nanoparticle suspension [0.5 mg mL^{-1} gold, 0.25 mM sodium dodecyl sulfate, 0.025 wt % Triton X-45 (Sigma-Aldrich)] was confined between the template and the stationary glass slide (gap ≈ 500 μm) and the patterned substrate was withdrawn underneath the droplet at a speed of 1 μm s^{-1} by a motorized translational stage (PLS-85, Physik Instrumente). Whereas the surfactants added tune surface tension and contact angle to enable selective deposition of the particles,[19] the elevated solution pH value (pH 9) in the case of insulin coating ensures colloidal stability by electrostatic repulsion. The experiment was carried at 12 K above dew point. Further experimental details can be found in Supporting Information Text T2. Prior to optical characterization, the samples were index-matched by spin-coating UV-curable PDMS at 2000 rpm for 60 s.

UV−Vis−NIR Spectroscopy. Optical spectra were measured on a Cary 5000 spectrometer (Agilent, USA) using the Cary universal measurement accessory. The spot size was fixed to 3 × 4 mm^2 for UV−vis and NIR detectors. All the dispersion spectra were measured

by rotating the sample plane by keeping the plane of incidence constant.

Bright-Field Imaging. Images of the self-assembled nanostructures were captured by a Nikon Eclipse LV100ND microscope using a bright-field reflection microscopy setup. The surface was illuminated by a halogen light source (12 V, 50 W) focused by a 5× objective lens. Images were taken by a Nikon DS-Fi2 5.24-megapixel charge coupled device (CCD) camera and analyzed by Nikon imaging (NIS-Elements) software. Unpolarized light was used for all the images.

Bright-Field Spectroscopy. Spectroscopy under strain was performed with a home-built stretching device on a transmission microscope (Nikon Ti-U). The microscope was equipped with an IsoPlane-160 spectrometer and a PIXIS: 256 CCD camera (Princeton Instruments). The light beam (100 W halogen lamp) was focused with a bright-field condenser (Ti-C-LWD) and collected with a 60× air objective (CFI S Plan Fluor ELWD, NA 0.7). Spectra with 383 nm bandwidths were taken at 600 and 750 nm center wavelength for 0.5 s (New Technologies and Consulting/Harald Giessen, NT&C software). All spectra were corrected by subtraction of the CCD's dark current and normalized by a reference spectrum, which was recorded in an area without particles.

Spectroscopic Ellipsometry. RC2-D dual rotating compensator ellipsometer, ex situ with automated tip and tilt alignment stage from J.A. Woollam Ellipsometer Solutions was used for refractive index measurements. Further, measured data were fitted with Complete Ease software via the Cauchy substrate model.

FDTD Simulations. We have used a commercial software package for performing FDTD simulations (Lumerical FDTD, version 8.16).[31] For the simulation of the optical response, a plane wave source was used and the frequency points were set to be half the wavelength span. Two-dimensional (2D) frequency-domain field and power monitors (transmission and reflection monitors in the direction parallel to the lattice plane) were used to obtain the optical responses of the system. For the dielectric properties of gold, data from Johnson and Christy were fitted using six coefficients with an rms error of 0.2.[32] The refractive index of the substrate (UV-PDMS) was measured via spectroscopic ellipsometry (Figure S6). In order to determine the electric field and surface charge density, we simulated the model at the LSPR and hybrid mode (SLR) frequencies. Periodic boundary conditions were used for square plasmonic lattice simulations in the lattice plane direction. For stretching, periodicities of the lattice in both the directions were increased based on the tabulated Poisson's ratio. All simulations reached an auto-shutoff of at least 10^{-7}. For the best simulation stability, the mesh area was chosen to be at least 100 nm larger than the existing structure in the lattice plane direction.

Atomic Force Microscopy. For evaluating the topography of photoresist masters and PDMS molds, atomic force microscopy (AFM) height images were measured using a Dimension 3100 NanoScope V (Bruker, USA) operated in tapping mode. Stiff cantilevers (40 N m^{-1}, 300 kHz, Tap300, Budget Sensors, and Bulgaria) were employed.

Scanning Electron Microscopy. A NEON 40 FIB-SEM workstation (Carl Zeiss Microscopy GmbH, Oberkochen, Germany) operated at accelerating voltage (electron high tension) of 1 kV was used for capturing scanning electron micrographs.

■ ASSOCIATED CONTENT

Ⓢ Supporting Information

The Supporting Information is available free of charge on the ACS Publications website at DOI: 10.1021/acsami.9b08871.

> Details on LIL, AFM of templates, TASA, hybridization model of SLR, comparison of quality factor, determination of fill factor, characterization of spacial order, mechano-tunability, in situ dark-field microscopy, and refractive index evaluation (PDF)

■ AUTHOR INFORMATION

Corresponding Authors
*E-mail: koenig@ipfdd.de (T.A.F.K.).
*E-mail: fery@ipfdd.de (A.F.).

ORCID
Jonas Schubert: 0000-0002-5728-9779
Tobias A. F. König: 0000-0002-8852-8752
Andreas Fery: 0000-0001-6692-3762

Author Contributions
‖Equal contribution: V.G., P.T.P.

Notes
The authors declare no competing financial interest.

■ REFERENCES

(1) Rycenga, M.; Cobley, C. M.; Zeng, J.; Li, W.; Moran, C. H.; Zhang, Q.; Qin, D.; Xia, Y. Controlling the Synthesis and Assembly of Silver Nanostructures for Plasmonic Applications. *Chem. Rev.* **2011**, *111*, 3669−3712.

(2) Chu, Y.; Schonbrun, E.; Yang, T.; Crozier, K. B. Experimental Observation of Narrow Surface Plasmon Resonances in Gold Nanoparticle Arrays. *Appl. Phys. Lett.* **2008**, *93*, 181108.

(3) Luk'yanchuk, B.; Zheludev, N. I.; Maier, S. A.; Halas, N. J.; Nordlander, P.; Giessen, H.; Chong, C. T. The Fano Resonance in Plasmonic Nanostructures and Metamaterials. *Nat. Mater.* **2010**, *9*, 707−715.

(4) Wang, W.; Ramezani, M.; Väkeväinen, A. I.; Törmä, P.; Rivas, J. G.; Odom, T. W. The Rich Photonic World of Plasmonic Nanoparticle Arrays. *Mater. Today* **2018**, *21*, 303−314.

(5) Kravets, V. G.; Kabashin, A. V.; Barnes, W. L.; Grigorenko, A. N. Plasmonic Surface Lattice Resonances: A Review of Properties and Applications. *Chem. Rev.* **2018**, *118*, 5912−5951.

(6) Hessel, A.; Oliner, A. A. A New Theory of Wood's Anomalies on Optical Gratings. *Appl. Opt.* **1965**, *4*, 1275−1297.

(7) Mayer, M.; Schnepf, M. J.; König, T. A. F.; Fery, A. Colloidal Self-Assembly Concepts for Plasmonic Metasurfaces. *Adv. Opt. Mater.* **2019**, *7*, 1800564.

(8) Tseng, M. L.; Yang, J.; Semmlinger, M.; Zhang, C.; Nordlander, P.; Halas, N. J. Two-Dimensional Active Tuning of an Aluminum Plasmonic Array for Full-Spectrum Response. *Nano Lett.* **2017**, *17*, 6034−6039.

(9) Volk, K.; Fitzgerald, J. P. S.; Ruckdeschel, P.; Retsch, M.; König, T. A. F.; Karg, M. Reversible Tuning of Visible Wavelength Surface Lattice Resonances in Self-Assembled Hybrid Monolayers. *Adv. Opt. Mater.* **2017**, *5*, 1600971.

(10) Yang, A.; Hryn, A. J.; Bourgeois, M. R.; Lee, W.-K.; Hu, J.; Schatz, G. C.; Odom, T. W. Programmable and Reversible Plasmon Mode Engineering. *Proc. Natl. Acad. Sci. U.S.A.* **2016**, *113*, 14201−14206.

(11) Steiner, A. M.; Mayer, M.; Seuss, M.; Nikolov, S.; Harris, K. D.; Alexeev, A.; Kuttner, C.; König, T. A. F.; Fery, A. Macroscopic Strain-Induced Transition from Quasi-Infinite Gold Nanoparticle Chains to Defined Plasmonic Oligomers. *ACS Nano* **2017**, *11*, 8871−8880.

(12) Kraus, T.; Malaquin, L.; Schmid, H.; Riess, W.; Spencer, N. D.; Wolf, H. Nanoparticle Printing with Single-Particle Resolution. *Nat. Nanotechnol.* **2007**, *2*, 570−576.

(13) Ni, S.; Wolf, H.; Isa, L. Programmable Assembly of Hybrid Nanoclusters. *Langmuir* **2018**, *34*, 2481−2488.

(14) Jiang, W.; Ma, Y.; Zhao, J.; Li, L.; Xu, Y.; Guo, H.; Song, L.; Chen, Z.; Zhang, Y. Robust Assembly of Colloidal Nanoparticles for Controlled-Reflectance Surface Construction. *ACS Appl. Mater. Interfaces* **2019**, *11*, 23773−23779.

(15) Sarkar, S.; Gupta, V.; Kumar, M.; Schubert, J.; Probst, P. T.; Joseph, J.; König, T. A. F. Hybridized Guided-Mode Resonances via Colloidal Plasmonic Self-Assembled Grating. *ACS Appl. Mater. Interfaces* **2019**, *11*, 13752−13760.

(16) Khlopin, D.; Laux, F.; Wardley, W. P.; Martin, J.; Wurtz, G. A.; Plain, J.; Bonod, N.; Zayats, A. V.; Dickson, W.; Gérard, D. Lattice Modes and Plasmonic Linewidth Engineering in Gold and Aluminum Nanoparticle Arrays. *J. Opt. Soc. Am. B* **2017**, *34*, 691.

(17) Auguié, B.; Barnes, W. L. Collective Resonances in Gold Nanoparticle Arrays. *Phys. Rev. Lett.* **2008**, *101*, 143902.

(18) Auguié, B.; Barnes, W. L. Diffractive Coupling in Gold Nanoparticle Arrays and the Effect of Disorder. *Opt. Lett.* **2009**, *34*, 401−403.

(19) Ni, S.; Leemann, J.; Wolf, H.; Isa, L. Insights into Mechanisms of Capillary Assembly. *Faraday Discuss.* **2015**, *181*, 225−242.

(20) Ni, S.; Klein, M. J. K.; Spencer, N. D.; Wolf, H. Capillary Assembly of Cross-Gradient Particle Arrays Using a Microfluidic Chip. *Microelectron. Eng.* **2015**, *141*, 12−16.

(21) Chanana, M.; RiveraGil, P.; Correa-Duarte, M. A.; Liz-Marzán, L. M.; Parak, W. J. Physicochemical Properties of Protein-Coated Gold Nanoparticles in Biological Fluids and Cells before and after Proteolytic Digestion. *Angew. Chem., Int. Ed.* **2013**, *52*, 4179−4183.

(22) Lowe, S.; O'Brien-Simpson, N. M.; Connal, L. A. Antibiofouling Polymer Interfaces: Poly(Ethylene Glycol) and Other Promising Candidates. *Polym. Chem.* **2015**, *6*, 198−212.

(23) Humphrey, A. D.; Barnes, W. L. Plasmonic surface lattice resonances on arrays of different lattice symmetry. *Phys. Rev. B: Condens. Matter Mater. Phys.* **2014**, *90*, 075404.

(24) Wang, D.; Bourgeois, M. R.; Lee, W.-K.; Li, R.; Trivedi, D.; Knudson, M. P.; Wang, W.; Schatz, G. C.; Odom, T. W. Stretchable Nanolasing from Hybrid Quadrupole Plasmons. *Nano Lett.* **2018**, *18*, 4549−4555.

(25) Danilov, A.; Tselikov, G.; Wu, F.; Kravets, V. G.; Ozerov, I.; Bedu, F.; Grigorenko, A. N.; Kabashin, A. V. Ultra-Narrow Surface Lattice Resonances in Plasmonic Metamaterial Arrays for Biosensing Applications. *Biosens. Bioelectron.* **2018**, *104*, 102−112.

(26) Bastús, N. G.; Comenge, J.; Puntes, V. Kinetically Controlled Seeded Growth Synthesis of Citrate-Stabilized Gold Nanoparticles of up to 200 nm: Size Focusing versus Ostwald Ripening. *Langmuir* **2011**, *27*, 11098−11105.

(27) Strozyk, M. S.; Chanana, M.; Pastoriza-Santos, I.; Pérez-Juste, J.; Liz-Marzán, L. M. Protein/Polymer-Based Dual-Responsive Gold Nanoparticles with pH-Dependent Thermal Sensitivity. *Adv. Funct. Mater.* **2012**, *22*, 1436−1444.

(28) Dewald, I.; Isakin, O.; Schubert, J.; Kraus, T.; Chanana, M. Protein Identity and Environmental Parameters Determine the Final Physicochemical Properties of Protein-Coated Metal Nanoparticles. *J. Phys. Chem. C* **2015**, *119*, 25482−25492.

(29) Höller, R. P. M.; Dulle, M.; Thomä, S.; Mayer, M.; Steiner, A. M.; Förster, S.; Fery, A.; Kuttner, C.; Chanana, M. Protein-Assisted Assembly of Modular 3D Plasmonic Raspberry-like Core/Satellite Nanoclusters: Correlation of Structure and Optical Properties. *ACS Nano* **2016**, *10*, 5740−5750.

(30) Matricardi, C.; Hanske, C.; Garcia-Pomar, J. L.; Langer, J.; Mihi, A.; Liz-Marzán, L. M. Gold Nanoparticle Plasmonic Superlattices as Surface-Enhanced Raman Spectroscopy Substrates. *ACS Nano* **2018**, *12*, 8531−8539.

(31) Lumerical Inc. Lumerical https://www.lumerical.com/products/fdtd-solutions/ (accessed Feb 10, 2019).

(32) Johnson, P. B.; Christy, R. W. Optical Constants of the Noble Metals. *Phys. Rev. B: Solid State* **1972**, *6*, 4370.